



Electron-beam-induced cracking in organic-inorganic halide Perovskite thin films



Srinivas K. Yadavalli, Min Chen, Mingyu Hu, Zhenghong Dai, Yuanyuan Zhou, Nitin P. Padture*

School of Engineering, Brown University, Providence, RI 02912, USA

ARTICLE INFO

Article history:

Received 9 April 2020

Revised 30 May 2020

Accepted 31 May 2020

Keywords:

Halide perovskites

Thin films

Scanning electron microscope

Grain boundaries

Fracture

ABSTRACT

The curious phenomenon of cracking in organic-inorganic halide perovskite (OIHP) thin films for solar cells during scanning electron microscopy (SEM) can be seen in literally thousands of published SEM micrographs. Here we demonstrate, for the first time, the mechanisms responsible for this *e*-beam-induced damage in OIHP thin films, which is precluding their detailed SEM-characterization and understanding. The *e*-beam-induced rapid volatilization of the organic species from the OIHP surface in the SEM results in localized shrinkage and buildup of tensile stresses. These stresses drive grain-boundaries cracking, resulting in a ‘mud-cracking’ pattern that is influenced by the thin-film grain size.

© 2020 Acta Materialia Inc. Published by Elsevier Ltd. All rights reserved.

Organic-inorganic halide perovskite (OIHP) materials are a fascinating class of true hybrid semiconductor materials [1], which are of great interest as active thin films in perovskite solar cells (PSCs) [2–4], and other optoelectronic devices such as light-emitting diodes, lasers, and detectors [5]. This is driven by the exceptional optoelectronic and defect properties of OIHPs that can be tuned [6–8]. The progress in PSCs has been particularly spectacular, where the record efficiency has soared from 3.8% [9] to 25.2% [10] over the past decade. The promise of low-cost, solution-processed PSCs with high efficiencies [11], and their potential impact on the global renewable-energy landscape, is driving the effort worldwide.

3D OIHPs have the general formula AMX_3 , where typically the organic-molecular cation ‘A’ is $CH_3NH_3^+$ (methylammonium, or MA^+) or $HC(NH_2)_2^+$ (formamidinium, or FA^+); ‘M’ is an elemental cation such as Pb^{2+} or Sn^{2+} ; and ‘X’ is a halide anion (I^- , Br^- , or Cl^-) [1,12]. The ‘A’ site can also be occupied by an elemental cation, such as Cs^+ , in all-inorganic halide perovskites, which are not OIHPs [1]. OIHP thin films used in PSCs are invariably polycrystalline due to the way they are solution- or vapor-processed [11]. The low formation energies of OIHPs that make it possible to process them at or near room temperature [11], also makes them unstable [13–15]. Furthermore, this renders OIHP thin films susceptible to electron-beam (*e*-beam) damage during

their observation in electron microscopes [16–20], making it difficult to characterize and understand the microstructures in any detail. This is very problematic because the microstructure is a dominant characteristic of OIHP thin films that controls, to a large extent, their physical, electrical, optical, and mechanical properties, which in turn influences PSCs performance, stability, and reliability [11,21–24]. Thus, it is critically important to understand the nature of *e*-beam damage in OIHPs, with the ultimate goal of mitigating it so as to enable detailed characterization and understanding of their microstructures.

Here we focus on *e*-beam degradation of OIHPs in the scanning electron microscope (SEM), a workhorse tool most widely used to characterize OIHP-thin-film microstructural features: grains (morphology, size, distribution), grain boundaries, etc. Cracking at grain boundaries in OIHP thin films is pervasive and has been observed in literally thousands of published SEM micrographs in the literature (see e.g. Ref. [25]). However, in almost all of the cases, this phenomenon is either not recognized as being associated with the very act of SEM observation or dismissed as an artifact or ignored altogether. Here we have performed a systematic SEM study of OIHP thin films of three different compositions – $MAPbI_3$, $FAPbI_3$, $MAPbBr_3$ – and one all-inorganic halide perovskite reference composition – $CsPb_{0.6}Sn_{0.4}I_3$. The effect of grain size on this phenomenon in $MAPbI_3$ and $FAPbI_3$ thin films is also investigated. We show that the genesis of cracking in OIHP thin films under the SEM *e*-beam is associated with the rapid volatilization of the organic cations from the exposed surface, resulting in tensile stresses. These tensile stresses drive the fracture of the grain

* Corresponding author.

E-mail address: nitin_padture@brown.edu (N.P. Padture).

boundaries resulting in patterns reminiscent of ‘mud-cracking’ associated with desiccation (drying) and/or thermal-expansion mismatch that are found in a wide range of systems, such as clay [26], ceramic glazes [27], thin films [28], coatings [29], geological formations [30], biological structures [31], etc.

All thin-film preparation and heat-treatments were performed inside a N_2 -filled glovebox, and all the synthesis/processing details are given in Supplementary Material (SM). Fine-grained MAPbI₃ thin films (~0.5 μm thickness) were prepared using a variation of the ‘solvent-engineering’ method [32]. A set of MAPbI₃ thin films with somewhat larger grains (medium-grained) were also prepared using a variation of the ‘solvent-vapor annealing’ method [33]. Medium-grained FAPbI₃ thin films (~0.5 μm thickness) were prepared using the ‘Lewis acid-base adduct’ method [34]. A set of coarse-grained FAPbI₃ thin films were prepared, also using the ‘solvent-vapor annealing’ method [23,35]. The ‘solvent-engineering’ method above was adapted for the preparation of fine-grained MAPbBr₃ thin films (~0.2 μm thickness) where the I⁻ is replaced by Br⁻. As an all-inorganic reference, fine-grained halide perovskite thin films (~0.25 μm thickness) of the composition CsPb_{0.6}Sn_{0.4}I₃ were prepared using a method described elsewhere [36]. This particular all-inorganic composition containing mixed Pb²⁺ and Sn²⁺ was chosen because of the relative ease of preparation of reasonable thickness thin films with high crystallinity and phase purity, as compared to the composition with only Pb²⁺ (CsPbI₃).

SEM (LEO 1530VP, Carl Zeiss, Germany or Quattro S ESEM, Thermo Fisher Scientific, USA) was used to characterize the top surfaces of all the thin films. The grain sizes of the MAPbI₃ and FAPbI₃ thin films were determined using the linear-intercept method on the SEM images, in conjunction with the ImageJ image-analysis software, where ~200 grains were used for each set of materials. Note that the naturally formed grooves (not deliberately revealed by etching) were assumed to represent the grain boundaries, which gives a reasonable estimation of the grain size in the thin films, although it can lead to some overestimation of the grain size in some cases [11,17,21]. The average grain size, \bar{D} , is given by $\alpha\bar{L}$, where \bar{L} is the measured average intercept length and α is a constant, which is taken to be 1.6 in the case of 3D microstructures assuming tetrakaidecahedral grains [37]. For grain size that is much larger than the thin-film thickness, the microstructure is essentially 2D, and it is more appropriate to assume the grains to be hexagonal prisms and not tetrakaidecahedrons. Assuming hexagonal prism grains geometry, we have derived the constant $\alpha=1.3$ (to be published). The SEM was also used to expose the thin films to *e*-beams of desired energies for different durations. In some cases, the images were recorded at regular intervals and merged to prepare video movies which are presented in SM.

A relatively large area of the MAPbBr₃ thin film (~0.1 mm²) was first exposed to *e*-beam (15 KV) in the SEM for several minutes. Conducting atomic force microscopy (C-AFM) of the region exposed to the *e*-beam and unexposed adjacent regions was performed using a commercial system (MFP3D Origin, Asylum Research, USA) in contact mode using a conducting Ti/Ir-coated Si tip (ASYLEEC.01-R2, Asylum Research, USA).

Figs. 1A–1B, 1C–1D, 1E–1F, and 1G–1H are SEM images (same magnification, same areas) of before (left) and after (right) *e*-beam exposure (15 KV, 2–3 min) of top surfaces of MAPbI₃, FAPbI₃, MAPbBr₃, and CsPb_{0.6}Sn_{0.4}I₃ thin films, respectively. Note that the ‘before’ images were taken on a fresh area with only a few seconds of *e*-beam exposure. Time-lapse movies of the cracking processes under 15 KV *e*-beam exposure in MAPbI₃, FAPbI₃, MAPbBr₃, and CsPb_{0.6}Sn_{0.4}I₃ thin films are presented in SM as Mov. S1, Mov. S2, Mov. S3, and Mov. S4, respectively. First consider fine-grained MAPbI₃ thin film case (avg. grain size ~0.3 μm), where cracking of random grain boundaries is seen in Fig. 1B, and the movie Mov. S1 shows that the cracking progresses with *e*-beam exposure du-

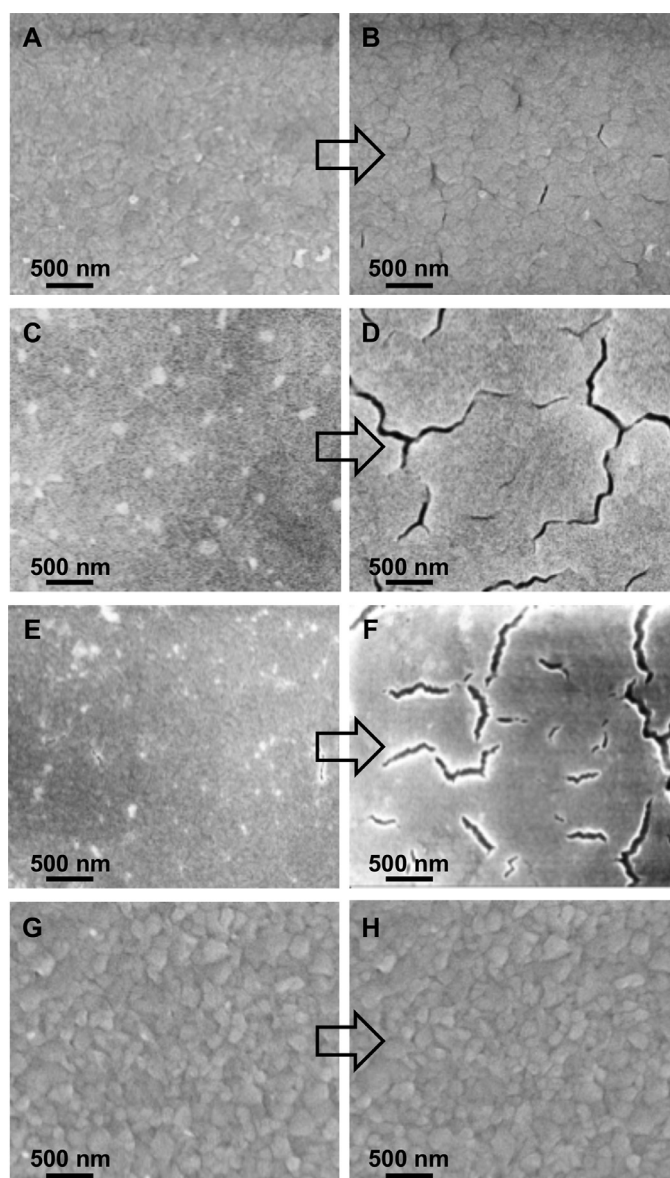


Fig. 1. Top-surface SEM images of thin films before (left) and after (right) SEM *e*-beam (15 KV) exposure for 2–3 min: (A–B) fine-grained MAPbI₃ OIHP, (C–D) medium-grained FAPbI₃ OIHP, (E–F) fine-grained MAPbBr₃ OIHP, and (G–H) fine-grained CsPb_{0.6}Sn_{0.4}I₃ perovskite. See corresponding time-lapse movies in SM: (Mov. S1) fine-grained MAPbI₃, (Mov. S2) medium-grained FAPbI₃, (Mov. S3) fine-grained MAPbBr₃, and (Mov. S4) fine-grained CsPb_{0.6}Sn_{0.4}I₃.

ration, accompanied by the widening of the crack opening. In the case of the medium-grained FAPbI₃ (avg. grain size ~0.6 μm), the grain-boundary cracking and linking is more pervasive (Fig. 1D). The movie in Mov. S2 shows the formation of ‘mud-cracking’ pattern with *e*-beam exposure duration. Note that not all grain boundaries have cracked, and much like the ‘mud-cracking’ pattern, there appears to be a characteristic size of the uncracked regions (~1.5 μm). This is more apparent in the fine-grained MAPbBr₃ case (avg. grain size ~0.1 μm) in Fig. 1F and Mov. S3. The notable exception is the fine-grained all-inorganic CsPb_{0.6}Sn_{0.4}I₃ thin film (avg. grain size ~0.3 μm), where no *e*-beam-induced cracking is observed in Fig. 1F and Mov. S4, and even after 10-min *e*-beam exposure (see Fig. S1 in SM). These results show direct correlation between the presence of organic cations (MA⁺, FA⁺) in the OIHP thin films and *e*-beam-induced grain-boundary cracking.

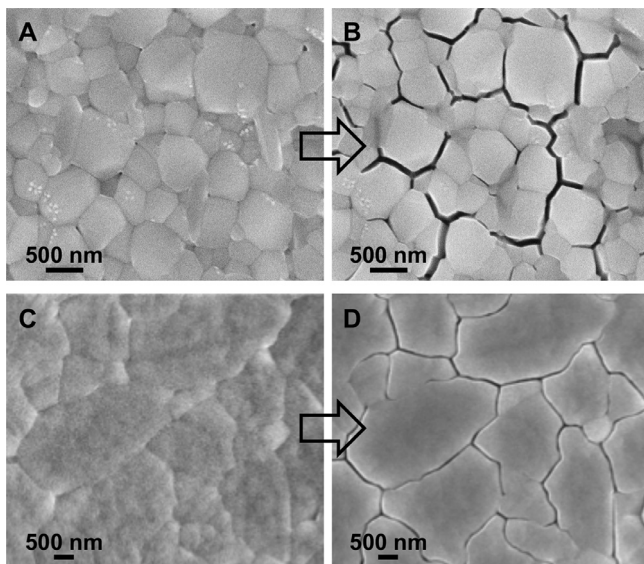


Fig. 2. Top-surface SEM images of OIHP thin films before (left) and after (right) SEM *e*-beam (15 KV) exposure for 2.5 min: (A–B) medium-grained MAPbI₃ OIHP and (C–D) coarse-grained FAPbI₃ OIHP. See corresponding time-lapse movies in SM: (Mov. S7) fine-grained MAPbI₃ and (Mov. S8) coarse-grained FAPbI₃.

Figs. S2A, S2B, and S2C in SM show SEM micrograph FAPbI₃ thin film exposed to *e*-beam for 3 min at 5 KV, 10 KV, and 15 KV, respectively. While grain-boundary cracking is observed in Figs. S2B and S2C, it is not apparent in Fig. S2A. These results show a clear effect of the *e*-beam energy and exposure duration. The corresponding time-lapse movies in Mov. S5 (5 KV) and Mov. S6 (10 KV) confirm this effect, although in Mov. S5 it can be seen that the grain boundaries become better defined (higher contrast) with increasing *e*-beam (5 KV) exposure.

Fine-grained MAPbI₃ thin films were exposed to *e*-beam (10 KV) in the SEM for a few minutes and subsequently the magnification was reduced slightly and images were recorded within seconds; Figs. S3A and S3B in SM present such SEM images. It can be seen that, while within the area exposed to *e*-beam there are grain-boundary cracks, extensive cracking envelopes that area, giving the appearance that the *e*-beam-exposed area has shrunk away from the rest of the thin film.

Fig. 2A–B and Fig. 2C–D are SEM images (same magnification, same areas) of before (left) and after (right) *e*-beam exposure (15 KV, 2.5 min) of top surfaces of medium-grained MAPbI₃ (avg. grain size ~0.6 μm) and coarse-grained FAPbI₃ (avg. grain size ~3.9 μm) thin films, respectively. Once again, the ‘before’ images were taken on a fresh area with only a few seconds of *e*-beam exposure. Comparing Figs. 1B and 2B in the case of MAPbI₃ thin films the effect of grain size is apparent. While grain-boundary cracking is limited in the fine-grained MAPbI₃ (avg. grain size ~0.3 μm) thin film, the ‘mud-cracking’ is more pronounced in its medium-grained counterpart under the same *e*-beam exposure conditions. The characteristic size of the uncracked region is still ~1.5 μm. In the case of coarse-grained FAPbI₃ thin film, each and every visible grain boundary appears to have cracked in Fig. 2D. Also observed in both the OIHP thin films in Fig. 2 is the surface smoothening induced by *e*-beam exposure. Time-lapse movies of the cracking processes in medium-grained MAPbI₃ and coarse-grained FAPbI₃ thin films are presented in SM as Mov. S7 and Mov. S8, respectively.

Based on these results the following mechanism for the *e*-beam-induced grain-boundary cracking in OIHP thin films is proposed. The high-energy SEM *e*-beam causes the partial volatilization of the organic species (MAI, FAI, MABr) from the OIHP structure on the surface [16–18,20]. The lack of *e*-beam-induced

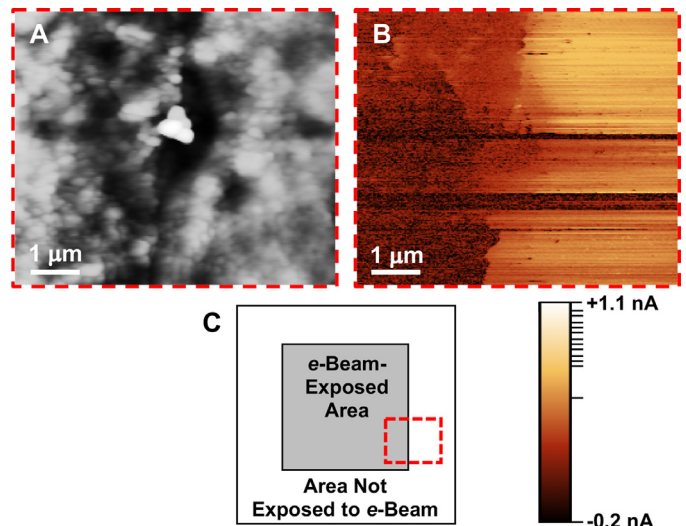


Fig. 3. Top-surface C-AFM images of fine-grained MAPbBr₃ OIHP thin film after prolonged SEM *e*-beam (15 KV) exposure: (A) topography and (B) electrical conductivity. (C) Schematic illustration showing the region (dashed red rectangle) imaged by C-AFM.

cracking in the all-inorganic CsPb_{0.6}Sn_{0.4}I₃ thin film (Fig. 1G and H, Fig. S1, Mov. S4) supports this hypothesis. Unfortunately, detecting quantitatively the loss of some of the organic cations from the surface is intractable using available characterization techniques such as X-ray photoelectron spectroscopy (XPS), X-ray diffraction (XRD), etc. Therefore, here we have resorted to an indirect non-destructive method of mapping the electrical conductivity of *e*-beam exposed and unexposed regions in the fine-grained MAPbBr₃ OIHP thin film using C-AFM. Fig. 3A and B show topography and electrical-conductivity maps from the region marked in Fig. 3C. The unexposed region has significantly higher electrical conductivity compared to the exposed region. This is attributed to the partial loss of MABr making the surface richer in Pb²⁺ and Br⁻ with a lower electrical conductivity. (The presence of PbBr₂ localized to the *e*-beam-exposed areas could not be confirmed.)

Inelastic scattering of electrons can result in damage via *e*-beam-induced heating of the specimen, given by [38]:

$$\Delta T = \frac{1.5 I_B V_0}{\pi k R}, \quad (1)$$

where I_B is the beam current, V_0 is the accelerating voltage, k is the thermal conductivity of the specimen, and R is the electron range (~1 μm). For the worst case scenario, with I_B ~100 pA and V_0 = 15 KV used here, and k ~0.3 W.m⁻¹.K⁻¹ for MAPbI₃ [39], the maximum ΔT is ~2.4 K. This temperature rise is negligible; hence specimen-heating can be ruled out as the cause for volatilization of the organic cations. Thus, inelastic-scattering radiolysis is most likely the *e*-beam damage mechanism in OIHPs, which has been observed in inorganic halides and organic materials, where surface-shrinkage occurs in the latter [38]. It is well known that radiolysis induced by *e*-beam involves excitation of the material followed by de-excitation, which can lead to bond breakages and volatilization of light elements (e.g. H, C, N) [38]. The increase in the *e*-beam damage observed with increasing accelerating voltage and exposure duration, (Fig. S2, Mov. S5, Mov. S6) which determines the total energy deposited into the specimen and the interaction volume, supports this hypothesis.

The loss of organic species from the *e*-beam-exposed surface of the OIHP thin film results in progressive volume shrinkage (Fig. 4), resulting in the buildup of localized biaxial tensile ‘drying’ stress, σ_D . It is worth noting that the volatilization appears to occur

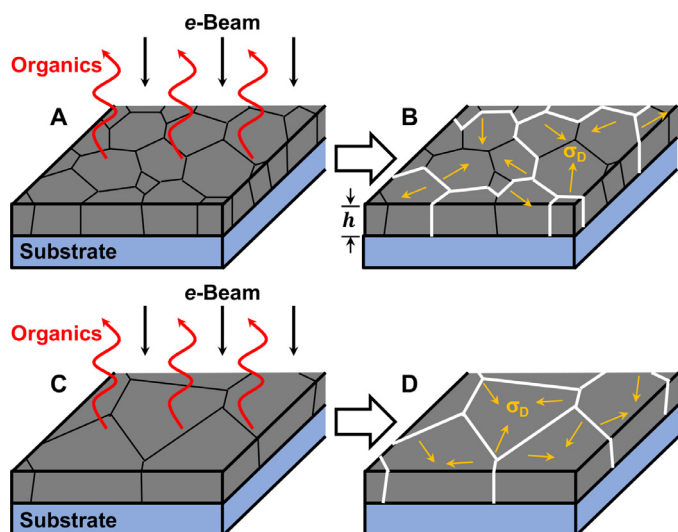


Fig. 4. Schematic illustration of mechanisms responsible for the *e*-beam-induced grain-boundary fracture and 'mud-cracking' pattern generation in OIHP thin films: (A–B) fine- and medium-grained and (C–D) coarse-grained. Not to scale.

uniformly from the thin-film surface, with only a mild preference for volatilization from the grain-boundary regions (see e.g. Mov. 5). This tensile stress reaches a critical value, σ_0 , which drives grain-boundary fracture when the mode I stress intensity factor, K , at the tip of a critical incipient flaw, c_0 , equals or exceeds the grain-boundary fracture toughness, K_{IC}^{GB} . Assuming that the incipient flaw scales with the film thickness, h , the critical condition for fracture is given by [28]:

$$K = K_{IC}^{GB} = \psi \sigma_0 (\beta h)^{0.5}, \quad (2)$$

where ψ and β are constants. This is likely to occur at several locations on the thin film, eventually leading to linking of the grain-boundary cracks to form the 'mud-cracking' pattern as *e*-beam exposure continues. The progressive widening of the crack opening observed in the movies (Movs. S1–S3 and Movs. S6–S8) in SM further support the idea of the volume shrinkage of the OIHP thin films with *e*-beam exposure. The details of the 'mud-cracking' process are quite complex and their modeling is rather involved [30]. But it has been shown that typically the equilibrium spacing between cracks, or the characteristic size of the uncracked 'cells,' λ , is $\sim 3h$ for compliant thin films on hard substrates [30]. This is because σ_D within the cell has relaxes well below σ_0 due to the surrounding cracking, and the available incipient cracks within the cell are smaller than c_0 . The net result is that Eq. (1) is not satisfied, precluding any cracking within the cell. In the medium-grained MAPbI₃ and FAPbI₃ thin films, $\lambda \sim 1.5 \mu\text{m}$ (Fig. 1D and 4B), which is $\sim 3h$. Since the coarse-grained α -FAPbI₃ thin film has the same thickness ($h \sim 0.5 \mu\text{m}$), λ is expected to $\sim 1.5 \mu\text{m}$, but that is much smaller than the average grain size ($\sim 3.9 \mu\text{m}$). This results in the cracking of each and every visible grain boundary in the coarse-grained FAPbI₃ thin film. Note that cracking within individual single-crystal grains is difficult because the incipient flaws are expected to be much smaller than those at the grain boundaries (βh), and the fracture toughness of the single-crystal grains is much higher than K_{IC}^{GB} [24]. These mechanisms of *e*-beam-induced grain-boundary cracking in OIHP thin films, and the effect of grain size, are depicted schematically in Fig. 4. It is worth mentioning that any pre-existing cracks in the OIHP thin films will open up spontaneously under SEM *e*-beam exposure, a phenomenon that has been exploited in our previous study to determine if closed cracks are actually healed [25].

Damage induced by *e*-beam in OIHP thin films is a serious concern, which is preventing the detailed characterization and understanding of their microstructures, holding back research progress in this important field. While the use of low-energy *e*-beams (e.g. ≤ 5 KV) and limiting the exposure to short periods of time (< 1 min) are obvious approaches for reducing *e*-beam damage, they are not real solutions and come at the cost of reduced characterization capabilities. Perhaps the best solution involves the development of more sensitive detectors for low-dose imaging, which is showing promise in the transmission electron microscopy (TEM) characterization of OIHPs [18,20], but has not been adapted to SEM as yet.

Declaration of Competing Interest

The authors declare that they have no known competing financial interests or personal relationships that could have appeared to influence the work reported in this paper.

Acknowledgement

The financial support for this research from the Office of Naval Research (grant# N00014-17-1-2232) and the National Science Foundation (grant# OIA-1538893) is gratefully acknowledged.

Supplementary materials

Supplementary material associated with this article can be found, in the online version, at doi:10.1016/j.scriptamat.2020.05.062.

References

- [1] B. Saparov, D.B. Mitzi, Chem. Rev. 116 (2016) 4558.
- [2] N.-G. Park, M. Grätzel, T. Miyasaka, Organic-Inorganic Halide Perovskite Photovoltaics: From Fundamentals to Device Architectures, Springer, Zurich, Switzerland, 2016.
- [3] H.J. Snaiith, Nat. Mater. 17 (2018) 372.
- [4] A.K. Jena, A. Kulkarni, T. Miyasaka, Chem. Rev. 119 (2019) 3026.
- [5] T.C. Sum, N. Mathews, Halide Perovskites: Photovoltaics, Light Emitting Diodes and Beyond, Wiley-VCH, Weinheim, Germany, 2019.
- [6] J.S. Manser, J.A. Christians, P.V. Kamat, Chem. Rev. 116 (2016) 12956.
- [7] T.M. Brenner, D.A. Egger, L. Kronik, G. Hodes, D. Cahen, Nat. Rev. Mater. 1 (2016) 15007.
- [8] Z. Xiao, Y. Yan, Adv. Energy Mater. 7 (2017) 1701136.
- [9] A. Kojima, K. Teshima, Y. Shirai, T. Miyasaka, J. Am. Chem. Soc. 131 (2009) 6050.
- [10] NREL, <https://www.nrel.gov/pv/cell-efficiency.html> (2019).
- [11] W.A. Dunlop-Shohl, Y. Zhou, N.P. Padture, D.B. Mitzi, Chem. Rev. 119 (2019) 3193.
- [12] D.B. Mitzi, in: K.D. Karlin (Ed.), Progress in Inorganic Chemistry, 48, John Wiley & Sons, New York, NY, 1999.
- [13] Y. Rong, Y. Hu, A. Mei, H. Tran, M.I. Saidaminov, S.I. Seok, M. McGehee, E.H. Sargent, H. Han, Science 361 (2018) 1214.
- [14] B.-W. Park, S.I. Seok, Adv. Mater. 31 (2019) 1805337.
- [15] C.C. Boyd, R. Cheacharoen, T. Leijtens, M.D. McGehee, Chem. Rev. 119 (2019) 3418.
- [16] N. Klein-Kedem, D. Cahen, G. Hodes, Acc. Chem. Res. 49 (2016) 347.
- [17] G.W.P. Adhyaksa, S. Brittan, H. Abolipš, A. Lof, X. Li, J.D. Keelor, Y. Luo, T. Duevski, R.M.A. Heeren, S.R. Ellis, D.P. Fenning, E.C. Garnett, Adv. Mater. 30 (2018) 1804792.
- [18] Y. Zhou, H. Sternlicht, N.P. Padture, Joule 3 (2019) 641.
- [19] Y. Li, W. Zhou, Y. Li, W. Huang, Z. Zhang, G. Chen, H. Wang, G.-H. Wu, N. Rolston, R. Vila, W. Chiu, Y. Cui, Joule 3 (2019) 2854.
- [20] J. Ran, O.O. Dyck, X. Wang, B. Yang, D.B. Geohegan, K. Xiao, Adv. Energy Mater. (2020) 1903191 in press.
- [21] Y. Zhou, O.S. Game, S. Pang, N.P. Padture, J. Phys. Chem. Lett. 6 (2015) 4827.
- [22] N. Rolston, A.D. Printz, J.M. Tracy, H.C. Weerasinghe, D. Vak, L.J. Haur, A. Priyadarshi, N. Mathews, D.J. Slotcavage, M.D. McGehee, R.E. Kalan, K. Zielinski, R.L. Grimm, H. Tsai, W. Nie, A.D. Mohite, S. Gholipour, M. Saliba, M. Grätzel, R.H. Dauskardt, Adv. Energy Mater. 8 (2018) 1702116.
- [23] S.K. Yadavalli, Z. Dai, M. Hu, Q. Dong, W. Li, Y. Zhou, R. Zia, N.P. Padture, Acta Mater. 193 (2020) 10.
- [24] Z. Dai, S.K. Yadavalli, M. Hu, M. Chen, Y. Zhou, N.P. Padture, Scr. Mater. 185 (2020) 47.
- [25] S.K. Yadavalli, Z. Dai, H. Zhou, Y. Zhou, N.P. Padture, Acta Mater. 187 (2020) 112.

- [26] L. Goehring, R. Conroy, A. Akhter, W.J. Clegg, A.F. Routh, *Soft Matter* 6 (2010) 3562.
- [27] W.D. Kingery, H.K. Bowen, D.R. Uhlmann, *Introduction to Ceramics*, Wiley Interscience, New York, 1976.
- [28] V.B. Shenoy, A.F. Schwartzman, L.B. Freund, *Intl. J. Fract.* 103 (2000) 1.
- [29] V. Lughy, V.K. Tolpygo, D.R. Clarke, *Mater. Sci. Eng. A* 368 (2004) 212.
- [30] L. Goehring, *Philos. Trans. A* 371 (2013) 20120353.
- [31] M.C. Milinkovitch, L. Manukyan, A. Debry, N. Di-Poi, S. Martin, D. Singh, D. Lambert, M. Zwicker, *Science* 339 (2013) 78.
- [32] N.J. Jeon, J.H. Noh, Y.C. Kim, W.S. Yang, S. Ryu, S.I. Seok, *Nat. Mater.* 9 (2014) 897.
- [33] Z.G. Xiao, Q.F. Dong, C. Bi, Y.C. Shao, Y.B. Yuan, J.S. Huang, *Adv. Mater.* 26 (2014) 6503.
- [34] J.-W. Lee, Z. Dai, C. Lee, H.M. Lee, T.-H. Han, N.D. Marco, O. Lin, C.S. Choi, B. Dunn, J. Koh, D.D. Carlo, J.H. Ko, H.D. Maynard, Y. Yang, *J. Am. Chem. Soc.* 140 (2018) 6317.
- [35] S.K. Yadavalli, Y. Zhou, N.P. Padture, *ACS Energy Lett.* 3 (2018) 63.
- [36] M. Hu, M. Chen, P. Guo, H. Zhou, J. Deng, Y. Yao, Y. Jiang, J. Gong, Z. Dai, Y. Zhou, F. Qian, X. Chong, J. Feng, R.D. Schaller, K. Zhu, N.P. Padture, Y. Zhou, *Nature Commun.* 11 (2020) 151.
- [37] A.R.C. Gerlt, A.K. Criner, L. Semiatin, E.J. Payton, *J. Am. Ceram. Soc.* 102 (2019) 37.
- [38] R.F. Egerton, P. Li, M. Malac, *Micron* 35 (2004) 399.
- [39] C. Ge, M. Hu, P. Wu, Q. Tan, Z. Chen, Y. Wang, J. Shi, J. Feng, *J. Phys. Chem. C* 122 (2018) 15973.